Nuclear Instruments and Methods in Physics Research A 832 (2016) 68–76

Contents lists available at ScienceDirect

Nuclear Instruments and Methods in Physics Research A

journal homepage: www.elsevier.com/locate/nima

Initial results from a multiple monoenergetic gamma radiography system for nuclear security

Buckley E. O'Day III[a,*], Zachary S. Hartwig[a,b], Richard C. Lanza[a], Areg Danagoulian[a]

[a] Department of Nuclear Science and Engineering, MIT, Cambridge MA 02139, USA
[b] Plasma Science and Fusion Center, MIT, Cambridge MA 02139, USA

ARTICLE INFO

Article history:
Received 29 February 2016
Received in revised form
23 May 2016
Accepted 27 May 2016
Available online 30 May 2016

Keywords:
Nuclear security
Shielded nuclear materials
Cargo container inspection
Gamma radiography
Active interrogation
Radiography

ABSTRACT

The detection of assembled nuclear devices and concealed special nuclear materials (SNM) such as plutonium or uranium in commercial cargo traffic is a major challenge in mitigating the threat of nuclear terrorism. Currently available radiographic and active interrogation systems use ~1–10 MeV bremsstrahlung photon beams. Although simple to build and operate, bremsstrahlung-based systems deliver high radiation doses to the cargo and to potential stowaways. To eliminate problematic issues of high dose, we are developing a novel technique known as multiple monoenergetic gamma radiography (MMGR). MMGR uses ion-induced nuclear reactions to produce two monoenergetic gammas for dual-energy radiography. This allows us to image the areal density and effective atomic number (Z_{eff}) of scanned cargo. We present initial results from the proof-of-concept experiment, which was conducted at the MIT Bates Research and Engineering Center. The purpose of the experiment was to assess the capabilities of MMGR to measure areal density and Z_{eff} of container cargo mockups. The experiment used a 3.0 MeV radiofrequency quadrupole accelerator to create sources of 4.44 MeV and 15.11 MeV gammas from the $^{11}\mathrm{B}(\mathrm{d},\mathrm{n}\gamma)^{12}\mathrm{C}$ reaction in a thick natural boron target; the gammas are detected by an array of NaI (Tl) detectors after transmission through cargo mockups . The measured fluxes of transmitted 4.44 MeV and 15.11 MeV gammas were used to assess the areal density and Z_{eff}. Initial results show that MMGR is capable of discriminating the presence of high-Z materials concealed in up to 30 cm of iron shielding from low- and mid-Z materials present in the cargo mockup.

Published by Elsevier B.V.

1. Introduction to gamma radiography in nuclear security

The field of nuclear security concerns itself with the challenges and dangers of nuclear weapons and materials. An increasing focus of the field is to mitigate the threat of nuclear terrorism, particularly the smuggling of special nuclear materials (SNM) or assembled nuclear devices in the commercial cargo traffic that passes through air, sea, rail, and road portals. Several technological developments have taken place over the last decade in the areas of passive interrogation, active interrogation, and transmission radiography to field systems which are capable of detecting such smuggling attempts.

Passive interrogation systems directly detect the natural radioactive signatures of fissionable and radioactive materials to determine whether an alarm should raised. While advantages of these systems include simplicity, low cost, and mobility, the main disadvantage is that most fissionable materials have low, difficult-to-detect rates of natural radioactive particle emission. The most intense signal is from weapons grade plutonium (WGP), which can produce fission neutrons at the rate of ~70 000 $\mathrm{s}^{-1}\,\mathrm{kg}^{-1}$. Even this high rate of emission can be successfully masked with small amount of hydrogenous shielding such as borated high density polyethylene (HDPE). Thus, passive detection systems are ineffective against low-emission nuclear materials, such as highly enriched uranium (HEU) and against competently shielded high-emission nuclear materials.

Nuclear threats in cargo that cannot be detected passively can be addressed with either active interrogation or transmission radiography. The key difference between the two techniques is that radiography measures the flux of primary particles in a beam that have been transmitted through the interrogated material while active interrogation measures the secondary particles produced in interactions between the primary particle beam and the interrogated material. Transmission radiography is the focus of the present work.

* Corresponding author.
E-mail address: buckley.oday@afit.edu (B.E. O'Day III).

http://dx.doi.org/10.1016/j.nima.2016.05.117
0168-9002/Published by Elsevier B.V.

1.1. Transmission radiography for container cargoes

The primary goal of research and development in transmission radiography for container cargoes is to achieve low dose, low cost, and high throughput systems that are sensitive to concealed and potentially shielded nuclear materials. To be practical, such systems must have short screening times in order to handle, for example, the approximately 57 000 ISO containers that enter the United States through its maritime ports every day [1].

An ANSI standard for cargo radiography, N42.46 [2], prescribes the required capabilities for radiographic systems, including cargo penetrability. The requirement states that a system claiming X cm penetration must produce a visually discernible transmission image of a steel object of 0.2X cm thickness shielded by X cm of steel equivalent. For example, a system that achieves this standard with areal densities of 150 g cm^{-2} for the cargo and 30 g cm^{-2} for the test object is classified to have a penetration of 150 g cm^{-2} /7.9 g cm^{-3} ≈ 19 cm of steel (cargo areal density divided by mass density of steel).

To achieve the performance required to clear commercial cargoes and assess the impact of a particular technique on the flow of commerce, it is important to consider the average densities of commercial cargoes. An effort to determine cargo contents and average densities has been previously performed [3]. The density was calculated by dividing the total container mass by the standardized volume of an ISO container, which provides a useful average density estimate although without details of local density variations. Fig. 1 shows the resulting frequency and the cumulative distribution of the densities. The results show that a radiographic system that can penetrate 20 cm steel equivalent (0.6 g cm^{-3} for an standard ISO container height of 240 cm) would clear 95% of the total cargo during primary inspection. For such a system, the remaining 5% will have to undergo secondary scanning before being manually inspected, in order to keep the total average screening times acceptable.

1.2. Present state of transmission radiography

Several transmission radiography and active interrogation techniques have been previously explored [4–6] and implemented into commercial systems. Most of the radiographic systems primarily use electron linear accelerators (linacs) to produce ~1–10 MeV bremsstrahlung photon beams. The traditional approach is to measure the integrated energy of a transmitted photon beam to produce an approximate reconstructed map of the areal density of the cargo. These systems are limited in their radiographic capabilities in several respects. The low duty factor (≤ 0.1%) of the linac results in a photon beam pulse that is significantly faster than the particle sensors – often $CdWO_4$ scintillator crystals with diode readouts and with scintillation decay times of ~16 μs. Thus, the sensors can operate only in integration mode, yielding no spectral information and limiting the ability to infer the cargo's atomic number. Another limitation of linac-based systems is that as the cargo thickness is increased, photon scattering significantly reduces radiographic image contrast for a fixed photon dose to the cargo. Recovering the image quality for thicker cargoes requires additional dose, which can approach 100 mRem per scan for cargo thicknesses of 40 cm steel. Finally, a large fraction of the bremsstrahlung photons are below ~3 MeV, which provide substantial dose to the cargo without contributing information on the cargo composition. For example, a system based on a 6 MeV electron beam would produce approximately 90% of the counts and 65% of the cargo dose from photons ≲3 MeV. While most details about dose-to-cargo in commercial radiographic systems are proprietary and not readily available, some insight can be gleaned from the available information. For example, the Cargo Advanced Automated Radiography System (CAARS) program involved the development of a radiographic system by L-3 Communications which delivered a dose of up to 65 miliRads to the container [7].

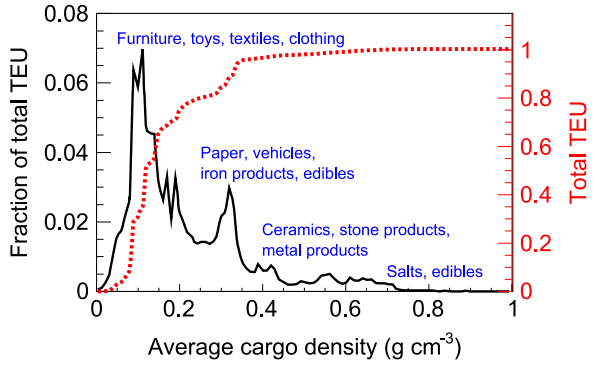

Fig. 1. The distribution of the average cargo density of shipping containers – specified in standardized shipping volume units of twenty-foot equivalent unit (TEU) – entering US ports during fourteen of the highest cargo volume days between July 2004 and June 2005. Annotations show the most important cargo and materials in regions of high frequency in the distribution. Figure adapted from [3].

A significant advance over traditional transmission radiography is achieved by the use of dual energy radiography, which allows us to estimate the effective atomic number (Z_{eff}) of the container cargo, allowing us to reveal the presence of high-Z shielding or concealed SNM. To determine Z_{eff}, the linac electron beam is switched between two energies, such as 4 MeV and 6 MeV, such that the difference in charge-integrated transmission at these two energies enables the estimation of effective atomic number in addition to areal density. As in the traditional systems, however, the use of charge integration, broad bremsstrahlung photon distributions and scatter contributions results in poor Z_{eff} sensitivity, requiring substantial additional doses to achieve an acceptably accurate measurement.

It should be noted that the above discussion focuses on the low duty, copper linac-based systems, which employ fan beams to achieve their radiographic objectives. These systems reflect the most commonly used technology in most cargo screening applications in the field, and as such are the focus of the comparison. A number of the limitations of the linac-based systems could be overcome by using continuous wave (CW) accelerators, and scanning containers by using bremsstrahlung photon pencil beams in a raster configuration. An example of such a system is the SmartScan 3D^{TM}, which fielded by Passport Systems, Inc. and is based on IBA TT100 CW 9 MeV accelerator [8].

Given the limitations of most bremsstrahlung-based radiography systems, achieving an alternative source of ~MeV photons would enable improvements in the detection of concealed nuclear materials while minimizing the imparted radiation dose. Ideally, the gamma source would be steady-state or continuous wave (CW) to achieve compatibility with standard gamma detectors that provide spectroscopic analysis [9] of the transmitted gamma flux. This would enable determination of both the density and Z_{eff} of the cargo. Furthermore, the source should produce monoenergetic gammas, which would eliminate degradation in the Z_{eff} sensitivity and enable energy-based suppression of contributions from scattered gammas.

2. Multiple monoenergetic gamma radiography

To alleviate high radiation dose and improve scan sensitivity as discussed in Section 1, we are developing a cargo screening technique known as multiple monoenergetic gamma radiography (MMGR). In contrast to conventional radiographic systems based

on electron-induced bremsstrahlung photons, MMGR uses ion accelerator-induced nuclear reactions to produce monoenergetic gammas and then exploits the energy-dependent physics of gamma interactions to assess both the areal density and Z_{eff} of the materials contained within the cargo. We note that other approaches to generating monoenergetic MeV photons have been proposed, usually on the basis of various laser techniques. The approach taken here provides the potential of multiple simultaneous monoenergetic gammas and is based more closely on existing commercial technologies.

2.1. Monoenergetic gamma production from nuclear reactions

The bombardment of low-Z targets by low-energy ($\lesssim 5$ MeV) light ions can be a prolific sources of monoenergetic $\lesssim$20 MeV gammas suitable for use in MMGR. Of special interest are compound nuclear reactions that lead to the decay of the residual nucleus through gamma emission, such as (p,nγ), (p, p$'\gamma$), (d,nγ), and (d,pγ). These reactions are favorable for four reasons. First, these reactions occur with almost all isotopes, providing a large selection of monochromatic gammas. Second, the reactions typically produce monoenergetic gammas at multiple energies, which is necessary for MMGR. Third, the reactions can have high differential cross sections (approaching $\gtrsim$100 millibarn per steradian in some cases), leading to the production of large gamma fluxes. Fourth, the reaction cross sections are relatively well characterized in the literature (*e.g.* [10–13]).

A candidate nuclear reaction for MMGR is the ^{11}B(d,nγ)^{12}C reaction [12]. The high reaction Q-value of $+13.73$ MeV enables deuterons above 1.63 MeV to excite the residual ^{12}C nucleus up to the 15.11 MeV state. The result is a strong flux of 4.44 MeV and 15.11 MeV, which are ideal for MMGR as discussed in Section 2.2, and significantly weaker fluxes at 10.67 MeV and 12.71 MeV, which are too small for use in the present application. Optimally produced with 3.0 MeV deuterons accessible to common radio-frequency quadrupole (RFQ), Van de Graaff, or electrostatic tandem accelerators, the 15.11 MeV gamma production cross section is maximized at approximately 1.0 millibarn per steradian at a forward angle relative to the beam [12] with the 4.44 MeV gamma production cross section roughly an order of magnitude higher. A competing gamma production reaction, ^{11}B(d,pγ)^{12}B, leads to the production monoenergetic gammas at 0.95 MeV and 1.67 MeV, which may be directly useful in MMGR or indirectly for detector calibration.

2.2. Exploiting gamma interaction physics

MMGR, like other gamma radiography methods, requires the use of strongly penetrating gammas such that container cargoes with areal densities in excess of 20 cm of steel equivalent (corresponding to an areal density of 158 g/cm^2) can be scanned in a reasonable time with practically accessible gamma fluxes. This necessitates the use of gammas with energies $\gtrsim$1 MeV. Depending on the atomic number of the material, the primary interaction of 1–5 MeV gammas with matter is Compton scattering, while above $\sim$5 MeV the interaction is dominated by electromagnetic pair production. Suitable nuclear reactions for MMGR, such as ^{11}B(d,nγ)^{12}C, are those which produce at least one gamma in the energy range where Compton scattering is dominant and one in the energy range where pair production is dominant. This allows the difference in Z-dependence between the Compton scattering and pair production cross sections to be exploited to assess the areal density and average Z of the container cargo.

The attenuation of a gamma beam through a homogeneous material (e.g. container cargo) can be approximated as

$$\frac{\Phi(E,X)}{\Phi(E,X=0)} = \exp(-\mu X) \tag{1}$$

where $X \equiv x\rho$ is the areal density of the volume, and μ is the mass attenuation coefficient of the material, and $\Phi(E,X)$ is the flux of gammas of energy E at a distance equivalent to X. A radiographic measurement would quantify the left side of Eq. (1), which, assuming a fixed value for μ, enables reconstruction of the areal density X. The mass attenuation coefficient, however, accounts for all possible interactions and consequently has a significant dependence on the gamma energy and the atomic number Z and atomic mass A of the material. Because the dominant processes involving gammas in the 1–10 MeV range for most elements are Compton scattering on orbital electrons and pair production on the nuclear Coulomb field, the mass attenuation coefficient can be written as

$$\mu = \mu_{cs} + \mu_{pp} = (Z\sigma_{cs} + \sigma_{pp})\frac{N_A}{A} \tag{2}$$

where σ_{cs} and σ_{pp} are the total cross sections for Compton scattering (CS) and pair production (PP), respectively, and N_A is Avogadro's number.

The mass attenuation coefficient for Compton scattering can be written

$$\mu_{cs} = \frac{Z}{A}N_A\sigma_{cs} \approx \sigma_{cs}N_A/2 \tag{3}$$

where the approximation $A/Z \approx 2$ was used. With Compton scattering occurring on orbital electrons, σ_{cs} and μ_{cs} are mostly insensitive to Z, and thus the total probability $\exp(-\mu_{cs}X)$ is only dependent on areal density. Compton scattering does have a significant dependence on gamma energy, however, following a $\sigma_{cs} \propto E_\gamma^{-1}$ power law at higher energies. This makes the $\sim$3–6 MeV energy range, where the sum of Compton and pair production cross sections is at its lowest for most higher Z materials, ideal for radiographing dense cargoes.

The mass attenuation coefficient of pair production can be written:

$$\mu_{pp} = \frac{N_A}{A}\sigma_{pp} \approx \frac{N_A}{A}Z^2 f(E_\gamma) \approx \frac{N_A}{2}Zf(E_\gamma) \tag{4}$$

where $f(E_\gamma)$ is a term with negligible Z dependence that can be calculated using the Born approximation with no nuclear screening [14]. In contrast to Compton scattering, the cross section of pair production has strong dependence on the nuclear charge Z, resulting in a linear Z dependence for the mass attenuation coefficient. For thin targets, the probability of attenuation by pair production $\exp(-\mu_{pp}X)$ varies linearly with Z and X, increases sublinearly with gamma energy E_γ, and is zero for $E_\gamma < 2m_e$. This results in gammas with energies in the range where pair production is dominant (e.g. $\sim$15 MeV) a powerful tool to reconstruct the material Z whose density can be determined from Compton scattering at lower gamma energies.

Compton scattering and pair production are by no means the only processes that take place at the energy scale of 1–6 MeV. Other photon interactions play a role too. These include various collective excitations, such as (γ, n) and other photonuclear reactions from light nuclei, nuclear resonance fluorescence (NRF), as well as such processes as Delbrük Scattering, nuclear Thompson scattering, and Rayleigh scattering. Some of these processes can involve very high cross sections over a very limited range of the energy-angle phase space (e.g. $\sim$10 barns for NRF, over the narrow range of $\sim$eV), their energy-averaged cross sections over the wider range of 1–6 MeV and scattering angles of 1° or more are small when compared to Compton and pair production cross sections, which together average to O(barn) and more.

In the 6–25 MeV range the physics of the interactions is augmented by the Giant Dipole Resonance (GDR). This process involves dipole oscillations of the nucleus' protons against the neutrons due to the electric field of the incident photon. For the deformed nuclei there can be two modes of oscillations, along the transverse and longitudinal axes of the deformation. The cross section of the resonance follows a Lorentz distribution, such that $\sigma \propto \Gamma^2E^2/((E^2 - E_m^2)^2 - \Gamma^2E^2)$, where E_m is the mode of the distribution, and Γ is the FWHM of the distribution. The total photoneutron cross sections as well as the cross sections for the individual final states (such as (γ, n), (γ, f) and higher multiplicity processes) have been measured and are reviewed in Ref. [15]. The authors in particular list the total maximum absorption cross sections $\sigma_m = \sigma(E_m)$ for a wide list of elements, in the range of $A \in (65, 209)$ (see Table IV in Ref. [15]). For example, for ^{65}Cu, ^{119}Sn, and ^{208}Pb the values for σ_m are 0.075, 0.253, and 0.654 barns, respectively. The pair production cross sections for these respective isotopes at their values of E_m can be determined from the literature [16]: these are 2.5, 6.7, and 15.2 barns. Thus, the GDR cross sections at most constitute only a ~3% correction to the total mass attenuation coefficients and can thus be neglected.

The physics basis for dual energy measurement in MMGR is presented graphically in Fig. 2, which shows the mass attenuation coefficient [16] for gammas in HDPE ($Z_{\text{eff}} \approx 2.5$), Fe ($Z=26$), Sn ($Z=50$), and U ($Z=92$). Between ~2 MeV and ~5 MeV, the mass attenuation coefficient (Compton scattering dominated) is roughly constant at 0.04 g cm^{-2} and independent of Z, differing between HDPE and U by only 10% at 2 MeV and 50% at 4.5 MeV. Above ~5 MeV, the mass attenuation coefficient (pair production dominated) has a linear Z dependence resulting in increasingly divergent values for higher Z materials. For example, at 15 MeV the mass attenuation coefficient for U is 1.4 greater than Sn, 1.9 greater than Fe, and 3.3 greater than HDPE. Thus, for gammas from the ^{11}B(d,nγ)^{12}C reaction considered in this work, the transmitted 4.44 MeV gammas (Compton scattering dominated) are only weakly Z-dependent and can be used to extract the approximate areal density; the transmission of 15.11 MeV gammas (pair production dominated) are strongly Z dependent and can be used to determine the Z of the cargo.

To simplify the measurement of Z_{eff} through cancellation of common systematic factors, MMGR utilizes the measured ratio of transmitted pair production-dominated gammas to Compton scattering-dominated gammas. For the ^{11}B(d,nγ)^{12}C reaction, the transmission ratio of 15.11 MeV to 4.44 MeV gammas is shown graphically in Fig. 3 as a function of areal density for materials ranging from aluminum ($Z=13$) to uranium ($Z=92$).

Several features of Fig. 3 are of note. First, the difference in Z-dependence between Compton scattering and pair production is evident in the transmission ratio value, enabling pure materials of different Z to be distinguished increasingly well for higher areal densities. Second, due to the concave shape of the mass attenuation curves as a function of energy, there will always be an inflection material ($Z=Z_i$) for which the attenuation coefficients of the two monoenergetic gammas are equal. For the 15.11 MeV and 4.44 MeV cases, this material is copper ($Z=29$). Third, for mixed material cargo, higher fractions of material with $Z > Z_i$ ($Z < Z_i$) relative to a single pure material will result in a decrease (increase) of the transmission ratio. This is important for understanding measurements of the transmission in real world cargo with complex material compositions.

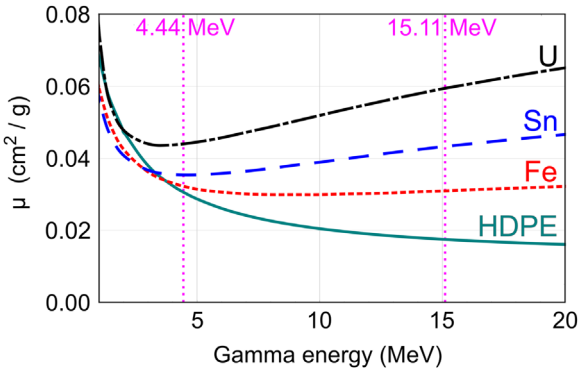

Fig. 2. Photon mass attenuation coefficients (μ) for 5% borated high density polyethylene (HDPE), iron (Fe), tin (Sn), and uranium (U). Data is from [17]. The vertical dashed lines show the 4.44 MeV and 15.11 MeV gammas produced in the ^{11}B(d,nγ)^{12}C reaction, a leading candidate reaction for multiple monoenergetic gamma radiography.

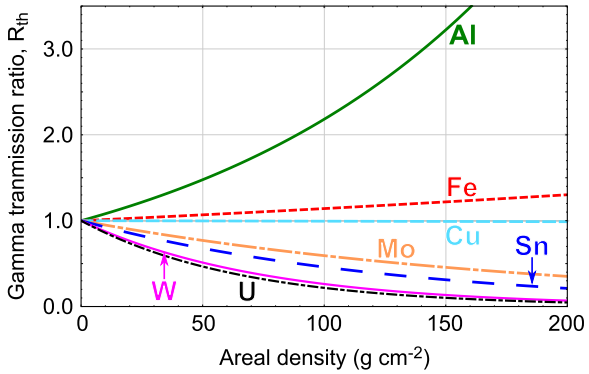

Fig. 3. Theoretical gamma transmission ratios for the 15.11 MeV to 4.44 MeV gammas produced in the ^{11}B(d,nγ)^{12}C reaction as a function of areal density for pure materials from Al ($Z=13$) to U ($Z=92$). The curves were calculated using Eq. (5).

2.3. A predictive model for cargo radiography

To better interpret experimental data and estimate transmission gamma ratio for any combination of materials, a simple predictive model is necessary. If we assume that a cargo is divided into M slabs of pure material m along the transmission axis then the theoretical transmission ratio, $\mathcal{R}_{\text{Th}}$, of two gammas – the 4.44 MeV and 15.11 MeV gammas generated by the ^{11}B(d,nγ)^{12}C reaction for example – can be calculated as

$$\mathcal{R}_{\text{Th}} = \frac{Y_{15.11}\cdot\epsilon_{i,15.11}\cdot\prod_{m=0}^{M}\exp\left(-X_m\mu_{m,15.11}\right)}{Y_{4.44}\cdot\epsilon_{i,4.44}\cdot\prod_{m=0}^{M}\exp\left(-X_m\mu_{m,4.44}\right)} \quad (5)$$

where Y is the total gamma yield, ϵ_i is the detector intrinsic efficiency, $X_m = \rho_m x$ is the areal density of material m, μ_m in the gamma mass attenuation coefficient of material m, and ρ_m is the mass density of material m; the subscripts 4.44 and 15.11 denote that the quantity should be evaluated at the respective gamma energy in MeV. The total gamma yield can be obtained either from the literature or calculated with available cross section data [18]. The detector intrinsic efficiency can either be experimentally measured or simulated; the mass linear attenuation coefficient is available in standard databases such as those provided by NIST [17]. Eq. (5) was used to generate the theoretical ratios for various materials as a function of areal density presented in Fig. 3.

3. Overview of the proof-of-principle experiment

To assess the capability of MMGR to measure the areal density and Z_{eff} of shielded materials within a container cargo mockup, we performed a series of proof-of-principle experiments at the MIT Bates Research and Engineering Center, located in Middleton, MA,

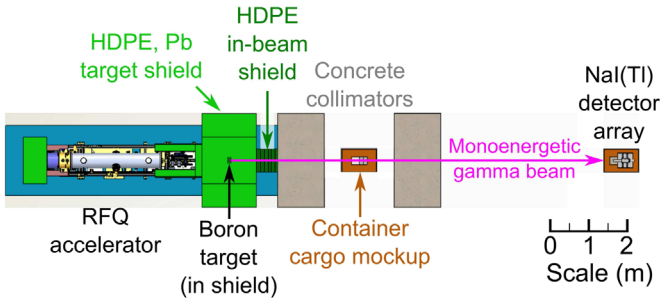

Fig. 4. A top-down view of a CAD representation of the multiple monoenergetic gamma radiography experiment at MIT Bates Research and Engineering Center. Note that the figure is to scale.

USA. This section provides a detailed overview of the experiment configuration hardware.

3.1. Experimental setup

The proof-of-principle MMGR experiment is depicted in Fig. 4. An accelerator (Section 3.2) generated 4.44 MeV and 15.11 MeV gammas via deuteron bombardment of a thick natural boron target. The target was enclosed by lead shielding and 5% borated high density polyethylene (B-HDPE) shield to minimize gamma and neutron radiation in the experimental hall. The lead shielding included a collimated 5.1 cm (2 in) wide beam port to collimate the gamma beam along the experimental beam axis. A 53.3 cm (21 in) B-HDPE in-beam shield was placed directly at the exit of lead collimator beam port. The in-beam shield minimized the flux of neutrons and undesirable neutron inelastic- and capture-induced gammas in the beam without significantly attenuating the 4.44 MeV and 15.11 MeV gammas.

Two concrete collimators along the beamline minimized scattered radiation in the experiment. Each collimator was composed of two large 122 cm (48 in) high density (5.9 g cm^{-3}) iron-concrete shield blocks centered on the beamline axis and separated by a narrow gap – the upstream collimator gap was 1.9 cm (0.8 in) and downstream collimator gap was 3.8 cm (1.5-in) gap. The container cargo mockup was positioned equidistant between the two concrete collimator sets and centered on the collimator gaps. A vertical array of gamma detectors (Section 3.2) was located after the downstream concrete collimator and surrounded by a 10.2 cm (4 in) lead shield to further shield the detectors from background gammas that did not come directly from the accelerator target.

The materials used in the container cargo mockups were aluminum (Al, $Z=13$), iron (Fe, $Z=26$), copper (Cu, $Z=29$), molybdenum (Mo, $Z=42$), tin (Sn, $Z=50$), tungsten (W, $Z=74$), and lead (Pb, $Z=82$). The materials were chosen to span a wide range of Z, from Al at $Z=13$ to Pb at $Z=82$, at roughly equivalent intervals to assess the MMGR capability of MMGR to determine the Z_{eff} of material in the cargo mockup. Each material was separately embedded in varying thicknesses of Fe and then measured to simulate the effect of shielding that could be present in real world SNM smuggling; the material configurations for all measurements are presented in detail in Section 5.

3.2. Accelerator and gamma detectors

The present MMGR ion accelerator is an Accsys Technologies Inc. DL-3 radiofrequency quadrupole (RFQ) linear accelerator. It was used to produce a pulsed, monoenergetic beam of 3.0 MeV deuterons. For all experimental measurements, the RFQ beam duty cycle was 0.25% with a beam pulse width of 25 μs and a repetition rate of 100 Hz. For the data production runs, the time-averaged beam current was between 9.0 μA and 14.5 μA. The beam target was a 2 mm thick natural boron film and was mounted on a forced air-cooled steel flange at the end of the beamline. Since the proof-of-principle experiments were not limited by time, these settings were chosen to ensure moderate count rates on the detector and to avoid melting the boron target. Upgrades to the data acquisition system and beam target since completed – coupled to the RFQ maximum duty cycle of 1.2% and >50 μA time-averaged current – enable substantially faster measurement times.

The gamma detectors were Saint-Gobain Crystals thallium-doped sodium iodide (NaI(Tl)) scintillators coupled to 2 in (5.1 cm) photomultiplier tubes. The NaI(Tl) crystals were 5.1 cm × 10.2 cm × 40.6 cm (2-in × 4-in × 16-in and encased in a 0.1 cm (0.04-in) thick stainless steel enclosure. Eight detectors were configured in a one-by-eight vertically stacked array configuration with the long 40.6 cm (16 in) axis of the detectors oriented along the beam line with the 10.2 cm (4 in) side perpendicular to the ground. For the data presented in this paper, a single detector was used to acquire data.

4. Data acquisition and analysis

As described in Section 2, MMGR fundamentally depends on quantifying the transmitted flux of 4.44 MeV and 15.11 MeV gammas incident on the NaI(Tl) detector. Doing so necessitates first acquiring and processing the acquired detector waveforms into calibrated energy spectra and then performing spectral analysis to extract the total 4.44 MeV and 15.11 MeV counts, which are finally converted to fluxes based on the experimental geometry and NaI(Tl) detector properties. This sections describes this process.

4.1. Data acquisition

The data acquisition system (DAQ) was composed of hardware from CAEN S.p.A. A V1724 VME digitizer board (100 megasamples/s; 14-bit; 8 channels) running standard CAEN firmware digitized the detector signals, which were stored for offline analysis. The V1724 was located within a CAEN VME8100 powered enclosure and readout to a nearby PC server via a CAEN V1718 USB-VME bridge board. The detectors were powered with two CAEN NDT1470 NIM high voltage units. Control of the DAQ hardware and offline analysis of the data was performed with the ADAQ Framework, an integrated toolkit for data acquisition and analysis of real and simulated radiation detectors [19].

A set of engineering runs was performed to optimize DAQ performance, ensuring that sufficient counting rate for good statistics was achieved in reasonable measurement time and that high-rate detection issues such as pileup and dead time were minimized. To provide insight into detector performance and the ability to apply post-processing waveform analysis algorithms to unmodified signals, 30 μs waveforms that captured the complete prompt burst of gammas from the 25 μs RFQ pulse were acquired. This long digital acquisition window was triggered with an analog timing pulse split from the RFQ ion source pulser unit. The complete waveforms were stored directly to disk and then post-processed first with a pileup rejection algorithm and then with a peak-finding algorithm that efficiently locates and separately integrates many peaks within one digital acquisition window into a calibrated NaI(Tl) gamma energy deposition spectrum.

4.2. Gamma spectra analysis

A representative NaI(Tl) gamma transmission spectrum is shown in Fig. 5. The 4.44 MeV gammas appear in the spectrum as a strong full energy peak at 4.44 MeV and the first escape peak at

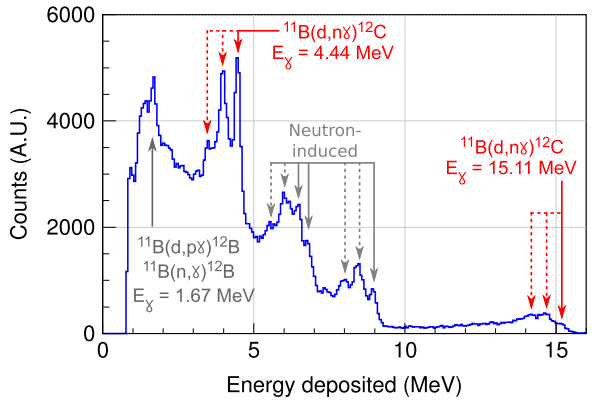

Fig. 5. A gamma transmission spectrum through 18.5 cm (7.3 in) of iron. The 4.44 MeV and 15.11 MeV gammas are shown in red. The 1.67 MeV gammas result from neutron capture on ^{11}B. The peaks at 6.7 MeV and 8.9 MeV are thought to results from various inelastic (n, n') reactions which occur near the target. While contributing a background to the 4.4 MeV region, these peaks can also be exploited in determining the cargo density and Z. Solid lines indicate full energy peaks; dashed lines indicate first and second escape peaks. (For interpretation of the references to color in this figure caption, the reader is referred to the web version of this paper.)

3.93 MeV; a suppressed second escape peak appears at 3.42 MeV due to the asymmetric shape of the NaI(Tl) detector, which makes double 0.511 MeV annihilation gamma escapes less likely. The continuum underneath the peaks – a combination of down-scattered high energy gammas and partial energy deposition in the detector – is computed using the sensitive nonlinear iterative peak-clipping (SNIP) algorithm [20] and subtracted. The residual spectrum is then integrated between 3.81 MeV and 4.66 MeV to determine the number of detector events due to 4.44 MeV gammas.

The detector response to 15.11 MeV gammas is a triplet of smeared full energy, first escape, and second escape peaks with a strong low-energy continuum. These features are caused by high energy electrons and positrons – created through pair production in the NaI(Tl) scintillator by the 15.11 MeV gammas – radiatively losing energy through bremsstrahlung emission that would otherwise have produced scintillation light. Without well-defined peaks for spectral analysis, the NaI(Tl) spectrum is simply integrated between 12.24 MeV and 15.50 MeV – an energy range where the only physically possible detectors interactions are due to 15.11 MeV gammas – in order to determine the number of detector events due to 15.11 MeV gammas.

Two other groups of monoenergetic gammas appear in Fig. 5. The first includes the 1.67 MeV gamma produced in the accelerator target via the ^{11}B(d,pγ)^{12}B reaction; the second includes gammas between ~6 MeV and ~9 MeV that are generated in neutron capture and inelastic reactions in the detector and ambient geometry in the experimental hall. At present, neither group is used in MMGR although we are assessing the feasibility of incorporating these gammas into the technique.

4.3. Detector intrinsic efficiency

The NaI(Tl) detector intrinsic efficiency, ϵ_i, must be known in order to convert the detector counts attributed to the 4.44 MeV and 15.11 MeV gammas into an incident gammas on the 5.1 cm × 10.2 cm (2 in × 4 in) detector face. ϵ_i for a gamma of energy E_γ can be defined as

$$\epsilon_i(E_\gamma) = \frac{\sum_{i=i_{low}}^{i_{high}} S(E)_i}{\text{Total } E_\gamma \text{ incident gammas}} \quad (6)$$

where $S(E)_i$ is the NaI(Tl) energy deposition spectrum histogram and i_{low} and i_{high} are the bin indices that define some energy range. The numerator represents the total counts in the energy spectrum within a user-defined energy range; the denominator represents all gammas of energy E_γ incident on the NaI(Tl) crystal. Traditionally, the numerator is defined as the counts under a gamma full energy peak centered at energy E_γ after subtraction of the underlying continuum; however, the numerator can be defined over any arbitrary energy range provided that the counts are directly attributable to gammas of energy E_γ. Using identical energy ranges to compute intrinsic efficiency and to analyze experimental data ensures a valid conversion from detector counts to incident gammas.

ϵ_i for 4.44 MeV and 15.11 MeV gammas were calculated using Geant4, a Monte Carlo particle transport code for modeling particle transport in matter [21]. A high fidelity model of the NaI(Tl) detector was implemented, including the crystal, stainless steel detector housing, and photomultiplier tube. Detector responses for 4.44 MeV and 15.11 MeV gammas were simulated. The energy deposited in and incident gammas on the NaI(Tl) crystal were scored. A Gaussian smearing was applied to the energy, to simulate the 8.1% (at 0.662 MeV) experimental energy resolution of the NaI(Tl) detector. The simulated events were then histogramed into energy spectra and analyzed identically to the experimental spectra to determine total number of detector events attributable to the 4.44 MeV and 15.11 MeV gammas as described in Section 4.2. Using an energy range of 3.81–4.66 MeV and 12.24–15.50 MeV for the as discussed in Section 4.2, the results were $\epsilon_i = 0.504 \pm 0.003$ for 4.44 MeV gammas and $\epsilon_i = 0.296 \pm 0.001$ for 15.11 MeV gammas.

5. Results and discussion

5.1. Validation of material Z and density effects on gamma spectrum

The Z-dependent and density-dependent effects of the material composition of the container cargo mockup – resulting from the 4.44 MeV and 15.11 MeV gammas interacting primarily via Compton scattering and pair production, respectively, as discussed in Section 2 – on the measured NaI(Tl) detector spectra are clearly evident in Figs. 6 and 7.

Fig. 6presents 4.44 MeV and 15.11 MeV gamma transmission spectra through single materials – Al, Fe, Cu, Mo, Sn, W, and Pb – that are arranged to have a fixed areal density of 126 g cm^{-2} with Z ranging from 13 to 82. Due to the equal areal densities and the insensitivity of the mass attenuation coefficient for the 4.44 MeV gamma, the counts attributed to the 4.44 MeV gammas remain

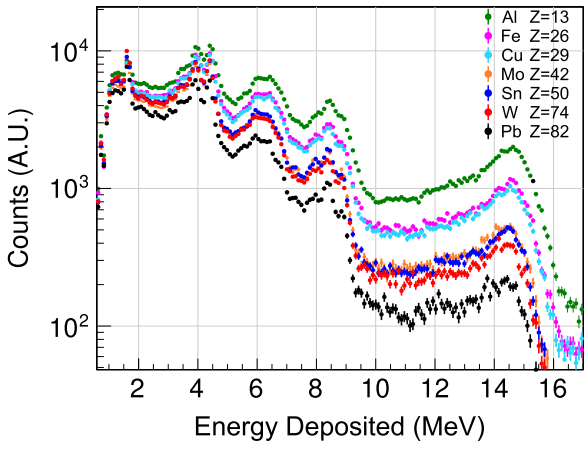

Fig. 6. Gamma transmission spectra for seven materials ranging from Al (Z=13) to Pb (Z=82), each with a total areal density of 126 g cm^{-2}.

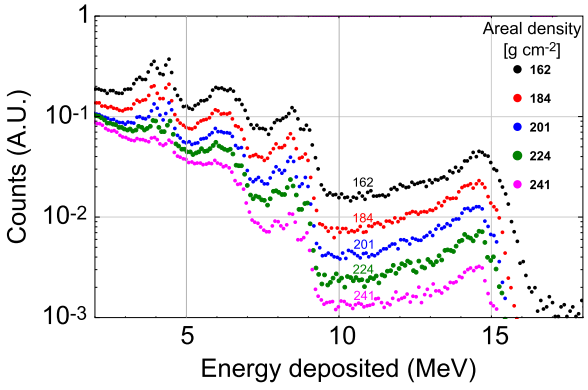

Fig. 7. Gamma transmission spectra for a single material (Fe, $Z=26$) at five areal densities ranging from 162 g cm^{-2} to 241 g cm^{-2}.

approximately constant for all materials. At the same time the counts attributed to the 15.11 MeV gammas decrease as the material Z increases – this is due to the $\sim Z^2$ dependence of the pair production cross section, which translates to an approximately $\propto Z$ dependence in mass attenuation coefficient.

Fig. 7 presents 4.44 MeV and 15.11 MeV gamma transmission spectra through materials of single Z (Fe, $Z=26$) but with areal densities ranging from 162 g cm^2 to 241 g cm^2. The dependence of 4.44 MeV gamma counts on the areal density is clear, showing the decreasing transmission in response to an increase in the areal density for fixed Z. The dependence of transmission of 15.11 MeV gammas on areal density in Fig. 6 simply follows an exponential attenuation described by the mass attenuation coefficient as expected.

5.2. Pure materials concealed in iron shielding

For container cargo composed of a heterogeneous mixture of materials, MMGR will measure the effective atomic number (Z_{eff}) of all materials traversed by the high energy gamma beam as it penetrates the cargo. We define Z_{eff} as

$$Z_{\text{eff}} = \frac{\sum_m^M Z_m \rho_m x_m}{\sum_m^M \rho_m x_m} \tag{7}$$

where ρ_m and x_m are the mass density and linear thickness of material m, respectively. Under this definition, Z_{eff} becomes the Z-weighted linear sum of areal-densities for all elementally pure materials m that compose the cargo.

In order to assess the sensitivity of MMGR to the Z_{eff} of the cargo at different areal densities, three experimental runs were conducted. Thirty three separate cargo mockups for each run were constructed by placing elementally pure materials ranging from Al ($Z=13$) to Pb ($Z=82$) – one material at a time – behind increasing thicknesses of Fe ($Z=26$) shielding to simulate the scanning of heavily shielded, smuggled cargo. A summary of the material configurations that made up the cargo mockups in each of the three experiment runs is shown in Table 1.

The pure materials were arranged to achieve a nominal areal density of 19.3 g cm^{-2} (Run 0), 49.0 g cm^{-2} (Run 1), and 68.3 g cm^{-2} (Run 2); the small discrepancies between the achieved and nominal areal densities were a result of limitations in available material thicknesses. The iron shielding areal density varied between 79–182 g cm^{-2} (Run 0), 59–139 g cm^{-2} (Run 1), and 40–120 g cm^{-2} (Run 2). A fixed areal density of 57 g cm^{-2} of 5% borated HDPE was present for all three runs to minimize neutron flux into the experimental hall; it was located between the incident gamma beam and the cargo mockup (see Fig. 4). Thus, total areal densities examined in these experiments were 155–255 g cm^{-2} (Run 0) and 165–245 g cm^{-2} (Runs 1 and 2).

Table 1
Material combinations that were used to create 33 cargo mockups to assess the sensitivity of MMGR to the effective atomic number of the cargo (See Eq. (7)). Seven pure materials – shown in the upper section – were chosen to span a wide range of atomic number. Shielding materials are shown in the lower section: Fe attempts to obscure the pure materials from detection; 5% borated HDPE is a neutron shield. Three separate experimental runs were performed with each run attempting to maintain a constant areal density for the pure materials: 19.3 g cm^{-2} for Run 0; 49.0 g cm^{-2} for Run 1; and 68.0 g cm^{-2} for Run 2.

Material	Atomic number	Density (g cm^{-3})	Areal density (g cm^{-2})		
			Run 0	*Run 1*	*Run 2*
Al	13	2.7	20.4	49.0	69.4
Fe	26	7.9	17.6	56.8	74.4
Cu	29	8.9	19.3	48.8	68.1
Mo	42	10.3	19.9	52.1	72.0
Sn	50	7.3	19.2	48.9	68.1
W	74	19.3	16.2	49.0	65.2
Pb	82	11.3	21.6	50.4	72.0
Fe	26	7.9	79–182	59–139	40–120
HDPE	~2.7	1.1	57	57	57

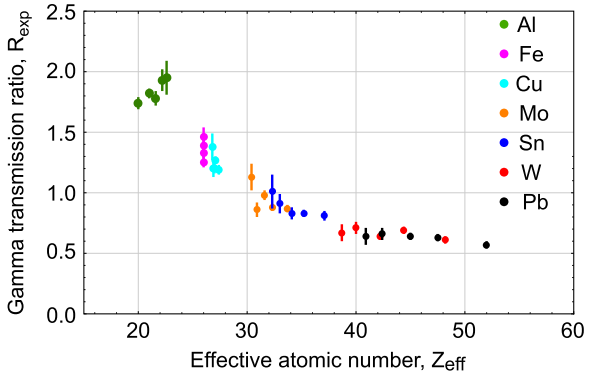

Fig. 8. Experimental transmission ratios of 15.11–4.44 MeV gammas for 33 cargo mockups (See Table 1, column "Run 1"). To form the mixed material cargo mockups, the elemental materials – noted in the figure legend – were shielded with increasing thicknesses of Fe; borated HDPE neutron shielding was also present in the beamline (See Fig. 4). The color code of the markers follows the elemental (pure) material at the base of the material-iron mix. The areal densities were 49.0 g cm^{-2} for the elemental materials, 59–139 g cm^{-2} for Fe shielding, and 57 g cm^{-2} for the HDPE. The Z_{eff} of each cargo mockup was calculated using Eq. (7) for the combinations of pure material, Fe shielding, and HDPE presented in Table 1. (For interpretation of the references to color in this figure caption, the reader is referred to the web version of this paper.)

5.2.1. Assessing Z discrimination capabilities

The Z_{eff} dependence of the ratio R_{exp} of counts in the 15.1 MeV and 4.4 MeV peaks is plotted in Fig. 8. As can be observed in the plot, as the pair production cross section increases rapidly with increasing atomic number, the transmission of 15.1 MeV photons is suppressed, when compared to that of the 4.4 MeV photons. This leads to the reduction of R_{exp} with increasing Z_{eff}. In addition to Z dependence, an areal density dependence is also present. While not shown explicitly in Fig. 8, the increasing areal density also changes R_{exp}. When observing R_{exp}'s dependence on Z_{eff} for various areal densities, it is clear in the data that at increased areal density the slope of R_{exp} vs. Z_{eff} is significantly larger.

The plot shows the predictive power of the ratio, indicating that cargo containing materials which have different Z_{eff} can be clearly distinguished using the 15.11 MeV to 4.44 MeV gamma ratio. For example, low-Z materials (*e.g.* Al at $Z=13$) stand out strongly from mid-Z materials (*e.g.* Fe at $Z=26$ and Mo at $Z=42$) and high-Z materials (*e.g.* W at $Z=74$). Discriminating materials closer in Z_{eff} becomes more challenging. To quantify the

Table 2
The figure of merit from Eq. (8) for discriminating between three areal densities of tin (Sn) and tungsten (W) shielded by increasing amounts of iron (Fe). Note that total areal density includes 57.0 g cm^{-2} of 5% borated HDPE neutron shielding.

Total areal density (g cm^{-2})	F.O.M. for Sn and W at areal densities of	
	49.0 g cm^{-2}	68.3 g cm^{-2}
165	5.55	6.26
175	–	–
185	4.95	4.71
195	–	–
205	4.24	3.88
215	–	–
225	2.48	2.23
235	–	–
245	2.37	1.36

technique's ability to discriminate between two materials we define the following figure of merit:

$$\text{F. O. M.} = \frac{|\mathcal{R}_0 - \mathcal{R}_1|}{\sqrt{\sigma_0^2 + \sigma_1^2}} \tag{8}$$

where $R_{0,1}$ are the measured ratios of transmitted gammas at 15.11 MeV and 4.44 MeV and $\sigma_{0,1}$ are the statistical uncertainties of the measured ratios for the two materials. Representing the number of standard deviations between two measurements, the F. O.M. sets the confidence with which two materials can be distinguished. For example, an F.O.M. of two provides 95% confidence in material discrimination.

Of particular interest in applying this technique to nuclear security is the ability to distinguish common, benign mid-Z material – such as copper or tin – in container cargo from potentially dangerous high-Z materials – such as uranium or plutonium. Table 2 presents the measured F.O.M. for distinguishing tin and tungsten (a proxy for high-Z fissile material) at three single material areal densities.

For tin and tungsten at areal densities of 49.0 g cm^{-2} and 68.3 g cm^{-2} embedded in increasing amount of iron, the technique discriminates the materials in all cases except one with better than 95% confidence level, a promising result given the large range of total areal density (165–245 g cm^{-2}). The result demonstrates that a ~3 cm thick high-Z material such as tungsten, uranium or plutonium could be distinguished from a mid-Z material such as tin despite more than 30 cm (11.8 in) of iron shielding in container cargo.

For the lowest areal density run of 19.3 g cm^{-2}, the high transmission resulted in exceedingly high count rates in the detectors, leading to pileup and subsequently to aberrations in the spectral information. Limitations in controls over beam current did not allow us to lower the later, which would have allowed us to reduce pileup rates. Thus, the data from the 19.3 g cm^{-2} runs is omitted in this work. Future research should focus on widening the range of beam current controls, and on pileup rejection algorithms. As a longer term goal a feedback algorithm can be developed which will vary the beam current based on detector rates. The later capability would not only reduce detector pileup rates, but also have the benefit of reducing the dose to cargo.

5.2.2. Validating the predictive gamma ratio model

In order to validate the predictive model presented in Section 2.3 for calculating gamma transmission ratios, the experimentally determined 15.11–4.44 MeV gamma ratios, R_{exp}, were compared to the theoretical ratios, R_{th}. The results appear in Fig. 9, which includes all three experimental runs at areal densities of 19.3 g cm^{-2}, 49.0 g cm^{-2}, and 68.1 g cm^{-2}. The model achieves very good agreement with the experimental results across a wide range of material areal density and Z_{eff}. This successful validation is important, as it provides a simple, computationally efficient, and accurate tool for the prediction of gamma transmission ratios for any arbitrary container cargo using MMGR. For example, this model could be used to simulate radiographic images created by large detector arrays and to rapidly identify Z_{eff} of each pixel in the image.

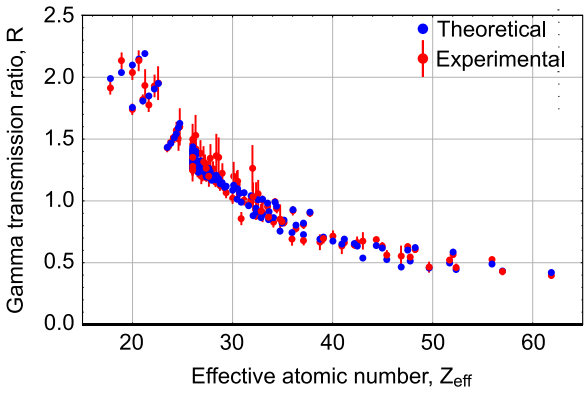

Fig. 9. A comparison between experimental and theoretical gamma transmission ratios as a function of effective atomic number for all three areal densities of 19.3, 49.0, and 68.3 g cm^{-2}. Experimental data is from the runs described in Table 1; theoretical values are predicted with Eq. (5).

6. Conclusion

A novel radiographic technique based on the transmission of gammas from nuclear reactions has been presented. The technique uses a high Q-value $^{11}B(d,n\gamma)^{12}C$ nuclear reaction triggered by a 3 MeV deuteron beam. This reaction generates 4.44 MeV and 15.11 MeV photons, which are then leveraged in a dual energy radiographic application. The proof of concept experiments, calculations, and preliminary analyses show the feasibility of this technique for distinguishing between low-, mid-, and high-Z materials in cargo configurations involving $\approx$30 cm of steel equivalents. The use of monochromatic photons is promising in that it will significantly reduce the dose to cargo in cargo screening applications, when compared to traditional linac bremsstrahlung based scanning applications currently used in the field, while achieving a high fidelity reconstruction of the effective atomic number of the cargo. Additionally, the source of 15.11 MeV gammas can be used to trigger photofission in most fissionable materials, along with other photonuclear processes, such as (γ, n) and (γ, $2n$). The fast neutrons emitted will then include various prompt and delayed fission signatures. Furthermore, the photons from the beta-decay of the neutron-rich daughter nuclei constitute another delayed signal which is unique to fissionable materials. Such delayed particles constitute a signal which can be used to detect shielded fissionable materials hidden in commercial cargoes.

Since the presented work only focused on proof of concept feasibility demonstration, significant improvements can be made to further improve the technique and broaden its applicability to real world cargo screening scenarios. Such improvements, as part of the future work, will need to focus on a number of areas of interest. Advanced algorithms and data mining techniques will need to be developed to make better use of transmitted photon flux data. The single detector measurements described in this work will be extended to the full radiographic array. The photon and neutron data contain significant amounts of auxiliary information relating to the cargo, such as neutron transmission and detection of photons from secondary electromagnetic processes, to further improve the assessment of cargo content. In the case of

former, a feasibility study has shown the usability of neutron beams in inferring the cargo content [22]. An important future direction involves the search for neutron-less nuclear reactions with higher cross sections for more optimal production of photons from nuclear reactions. Finally, the use of delayed photofission signatures for the detection of shielded hidden fissionable materials is of particular promise.

The application of multiple monochromatic gamma radiography using alternative ion accelerator platforms is another important area of future research. The research presented in the paper employed a 3 MeV RFQ accelerator, which is optimal for research and development purposes. An accelerator which has smaller footprint and a higher duty factor is necessary for deployable applications, however. Over the last decade there has been a significant progress in the development of compact, high duty factor medical cyclotrons. While primarily used for medical isotope production, such platforms may be suitable for MMGR. An example of such a machine is the ION-12SC, a 12.5 MeV proton superconducting cyclotron [23,24]. ION-12SC and subsequent higher energy proton and deuteron cyclotrons will allow in the future to trigger a variety of nuclear reactions which produce gammas with a potential for use in new MMGR embodiment. Some examples of reactions of interest are: $^{12}C(p, p'\gamma)^{12}C$, which does not produce neutrons and emits gammas with energies of 4.4 MeV, 7.7 MeV, and 9.6 MeV; $^{16}O(p, p'\gamma)^{16}O$, producing gammas with energies of 6.1 MeV and 8.9 MeV. The possibility and practicality of using these alternative reactions will be part of the future research effort.

Acknowledgments

This work is supported in part by the U.S. Department of Homeland Security Domestic Nuclear Detection Office under a competitively awarded collaborative research ARI-LA Award, ECCS-1348328 and is part of a collaboration between MIT, Georgia Institute of Technology and Pennsylvania State University. This support does not constitute an express or implied endorsement on the part of the Government. The authors would like to thank Ernest Ihloff, Peter Binns, Hamid Moazeni, as well as the rest of the staff at the Bates Laboratory, for their generous support. The authors are grateful to T.D. MacDonald for his help in data analysis, to Richard Sheffield (LANL) and our colleagues at Georgia Institute of Technology, Pennsylvania State University, and University of Michigan for useful discussions and advice.

References

[1] R. Kouzes, J. McDonald, D. Strachan, S. Bowyer, Radiation Detection and Interdiction at U.S. Borders, Oxford University Press, New York, 2011.
[2] American National Standard for Determination of the Imaging Performance of X-ray and Gamma-ray systems for Cargo and Vehicle Security Screening, ANSI N42.46–2008, 2008, pp. 1–26.
[3] M.A. Descalle, D. Manatt, D. Slaughter, Analysis of Recent Manifests for Goods Imported Through US Ports, Lawrence Livermore National Laboratory Report UCRL-TR-225708, 2006.
[4] A. Danagoulian, et al., Prompt neutrons from photofission and its use in homeland security applications, in: 2010 IEEE International Conference on Technologies for Homeland Security (HST), IEEE, Billerica, MA, pp. 379–384.
[5] R. Ledoux, W. Bertozzi, Methods and systems for determining the average atomic number and mass of materials, US Patent 7,286,638, 2007.
[6] W. Bertozzi, R.J. Ledoux, Nuclear resonance fluorescence imaging in non-intrusive cargo inspection, Nucl. Instrum. Methods Phys. Res. Sect. B: Beam Interact. Mater. At. 241 (2005) 820–825, The Application of Accelerators in Research and Industry Proceedings of the Eighteenth International Conference on the Application of Accelerators in Research and Industry (CAARI 2004) Eighteenth International Conference on the Application of Accelerators in Research and Industry.
[7] D. Perticone, Personal Communications, 2016. L-3 Communications.
[8] Smartscan 3d^{TM}, ⟨http://www.passportsystems.com/pg/products/smartscan-3d⟩, 2015.
[9] A.J. Gilbert, B.S. McDonald, S.M. Robinson, K.D. Jarman, T.A. White, M. R. Deinert, Non-invasive material discrimination using spectral x-ray radiography, J. Appl. Phys. 115 (2014).
[10] Z. Elekes, A.Z. Kiss, I. Biron, T. Calligaro, J. Salomon, Thick target gamma-ray yields for light elements measured in the deuteron energy interval of 0.7–3.4 meV, Nucl. Instrum. Methods Phys. Res. Sect. B: Beam Interact. Mater. At. 168 (2000) 305–320.
[11] G. Sziki, A. Simon, Z. Szikszai, Z. Kertész, E. Dobos, Gamma ray production cross-sections of deuteron induced nuclear reactions for light element analysis, Nucl. Instrum. Methods Phys. Res. Sect. B: Beam Interact. Mater. At. 251 (2006) 343–351.
[12] T.N. Taddeucci, R.L. Sheffield, T.N. Massey, D. Carter, J.E. O'Donnell, C.R. Brune, D. Ingram, D. Jacobs, A. DiLullo, Neutron and Gamma-ray Production with Low-energy beams, Los Alamos National Laboratories Report LA-UR-07-2724, 2007.
[13] Y. Wang, M. Nastasi (Eds.), Handbook of Modern Ion Beam Materials Analysis, 2nd edition,Materials Research Society, Warrendale, PA, 2010.
[14] W. Leo, Techniques for Nuclear and Particle Physics Experiments, Springer-Verlag, Berlin Heidelberg, 1994.
[15] B. Berman, S. Fultz, Measurements of the giant dipole resonance with monoenergetic photons, Rev. Mod. Phys. 47 (1975).
[16] Xcom: Photon Cross Sections Database, ⟨http://www.nist.gov/pml/data/xcom/index.cfm⟩, 2015. National Institute of Standards and Technology.
[17] S.M. Seltzer, Calculation of photon mass energy-transfer and mass energy-absorption coefficients, Radiat. Res. 136 (1993) 147–170.
[18] R. Mateus, A. Jesus, J. Ribeiro, A code for quantitative analysis of light elements in thick samples by PIGE, Nucl. Instrum. Methods Phys. Res. Sect. B: Beam Interact. Mater. At. 229 (2005) 302–308.
[19] Z.S. Hartwig, The ADAQ framework: an integrated toolkit for data acquisition and analysis with real and simulated radiation detectors, Nucl. Instrum. Methods Phys. Res. Sect. A: Accel. Spectrom. Detect. Assoc. Equip. 815 (2016) 42–49.
[20] M. Morháč, J. Kliman, V. Matoušek, M. Veselský, I. Turzo, Efficient one- and two-dimensional gold deconvolution and its application to γ-ray spectra decomposition, Nucl. Instrum. Methods Phys. Res. Sect. A: Accel. Spectrom. Detect. Assoc. Equip. 401 (1997) 385–408.
[21] S. Agostinelli, et al., Geant4–a simulation toolkit, Nucl. Instrum. Methods Phys. Res. Sect. A: Accel. Spectrom. Detect. Assoc. Equip. 506 (2003) 250–303.
[22] J. Rahon, A. Danagoulian, T.D. MacDonald, Z.S. Hartwig, R.C. Lanza, Spectroscopic neutron radiography for a cargo scanning system, Nucl. Instrum. Methods Phys. Res. Sect. A: Accel. Spectrom. Detect. Assoc. Equip. 820 (2016) 141–145.
[23] V. Smirnov, S. Vorozhtsov, J. Vincent, Design study of an ultra-compact superconducting cyclotron for isotope production, Nucl. Instrum. Methods Phys. Res. Sect. A: Accel. Spectrom. Detect. Assoc. Equip. 763 (2014) 6–12.
[24] T. Antaya, Compact, Cold, Superconducting Isochronous Cyclotron, US Patent 8,558,485, 2013.